The Astrophysical Journal Letters, 998:L40 (13pp), 2026 February 20 https://doi.org/10.3847/2041-8213/ae3d2e


# Pulsations Change the Structures of Massive Stars before Explosion: Interpreting SN 2023ixf and SN 2024ggi

Eva Laplace[1,2,3,4], Vincent A. Bronner[4,5], Fabian R. N. Schneider[4,6], and Philipp Podsiadlowski[7,4,8]
[1] Institute of Astronomy, KU Leuven, Celestijnenlaan 200D, B-3001 Leuven, Belgium; eva.laplace@kuleuven.be
[2] Leuven Gravity Institute, KU Leuven, Celestijnenlaan 200D, box 2415, 3001 Leuven, Belgium
[3] Anton Pannekoek Institute of Astronomy, University of Amsterdam, Science Park 904, 1098 XH Amsterdam, The Netherlands
[4] Heidelberger Institut für Theoretische Studien, Schloss-Wolfsbrunnenweg 35, 69118 Heidelberg, Germany; vincent.bronner@h-its.org
[5] Universität Heidelberg, Department of Physics and Astronomy, Im Neuenheimer Feld 226, 69120 Heidelberg, Germany
[6] Astronomisches Rechen-Institut, Zentrum für Astronomie der Universität Heidelberg, Mönchhofstrasse 12-14, 69120 Heidelberg, Germany
[7] London Centre for Stellar Astrophysics, Vauxhall, London, UK
[8] University of Oxford, St Edmund Hall, Oxford, OX1 4AR, UK
*Received 2025 September 3; revised 2026 January 23; accepted 2026 January 23; published 2026 February 17*

## Abstract

Massive red supergiants (RSGs) are known to become hydrodynamically unstable before they explode. Still, the vast majority of supernova (SN) models assume RSG progenitors in hydrostatic equilibrium. Here we follow the hydrodynamic evolution of RSGs with different masses and the development of radial envelope pulsations. Pulsations significantly alter the observable pre- and post-SN properties, and their importance increases substantially as a function of initial mass. We demonstrate that inferring core masses, let alone initial masses, from a single pre-SN luminosity and effective temperature of high-mass RSGs is inadvisable, as these can vary by an order of magnitude during the pulsation. We find that pulsations can naturally lead to "early-excess" emission in SN light curves and to variations in early photospheric velocities, which can help break degeneracies in Type II SNe. We compare to SN 2023ixf and SN 2024ggi, for which pulsating RSG progenitors were reported. We demonstrate that the pre- and post-SN characteristics of SN 2023ixf agree very well with our exploding pulsating RSG model and exhibit meaningful differences from hydrostatic models. The data coverage is insufficient to break all degeneracies. We find insufficient evidence for the claimed pulsation period of the SN 2024ggi progenitor, as it matches Spitzer's orbital period. This study underscores the importance of hydrodynamical pre-SN stellar models, in particular for massive stars from $\gtrsim$15 $M_{\odot}$. It implies an important shift in our understanding of the last stages of massive star evolution, the interpretation of pre-SN properties, the connection between SNe and their progenitors, and the missing RSG problem.

*Unified Astronomy Thesaurus concepts:* Stellar evolution (1599); Red supergiant stars (1375); Hydrodynamics (1963); Stellar pulsations (1625); Supernovae (1668); Core-collapse supernovae (304); Type II supernovae (1731)

## 1. Introduction

The final life of massive stars is poorly constrained. This last phase of the evolution after core helium burning lasts only on the order of thousands to tens of thousands of years, which means that it is rare to find stars in this evolutionary stage observationally. Their properties in this last stage are particularly uncertain. Single stars with masses from ≈8 to ≈25 $M_{\odot}$ are expected to end their lives as luminous red supergiants (RSGs). While supernova (SN) observations point to growing evidence for dense circumstellar material (CSM) near SNe inferred from narrow, flash ionization emission features in their early spectra (A. Gal-Yam et al. 2014; R. J. Bruch et al. 2021), early excess in SN light curves (LCs; V. Morozova et al. 2018; K. R. Hinds et al. 2025), and late-time radio, infrared, and X-ray emission of nearby SNe (N. N. Chugai et al. 2007; C. Fransson et al. 2014), observationally inferred mass-loss rates of RSGs are orders of magnitude lower (B. Davies et al. 2018; M. Yang et al. 2018, 2023; E. R. Beasor et al. 2020; K. Antoniadis et al. 2024; L. Decin et al. 2024). In addition, massive RSGs are highly variable (L. L. Kiss et al. 2006; J. R. Percy & V. C. Khatu 2014), likely due to radial envelope pulsations (R. Stothers 1969; R. Stothers & K. C. Leung 1971; A. Heger et al. 1997; S.-C. Yoon & M. Cantiello 2010). Their period–luminosity (PL) relations have been used to infer the distances to other galaxies (e.g., J. S. Jurcevic et al. 2000). However, most SN explosion models rely on progenitors assumed to be in hydrostatic (HS) equilibrium.

The discovery of SN 2023ixf (K. Itagaki 2023) and its pulsating RSG progenitor (e.g., C. D. Kilpatrick et al. 2023) puts the validity of this assumption into question. This hydrogen-rich (Type II) SN (D. A. Perley et al. 2023), located in the Pinwheel galaxy, M101, at a distance of 6.85 ± 0.15 Mpc, is among the closest SNe to have occurred in the past decade. At the location of the SN, archival searches revealed a variable RSG progenitor with a pulsation period of 1100 days (J. E. Jencson et al. 2023; C. D. Kilpatrick et al. 2023; Z. Niu et al. 2023; M. D. Soraisam et al. 2023; Y.-J. Qin et al. 2024; C. L. Ransome et al. 2024; S. D. Van Dyk et al. 2024; D. Xiang et al. 2024b). Given the close proximity of the SN, it has led to a wealth of observations across the electromagnetic spectrum. Several studies reported evidence for CSM close to the SN (e.g., W. V. Jacobson-Galán et al. 2023; J. E. Jencson et al. 2023; N. Smith et al. 2023; E. A. Zimmerman et al. 2024). In addition, there are several signs of possible large-scale asymmetries in the ejecta, which have been interpreted as a signature of past outflows or binary interactions (A. Singh et al. 2024; M. Shrestha et al. 2025; S. S. Vasylyev et al. 2025). For interpreting the properties of this object, few studies have taken the pulsation of the progenitor into account. A notable exception is the work by

B. Hsu et al. (2024), who proposed to only select stellar models consistent with the pulsation period to break degeneracies in the explosion properties.

More recently, another close-by H-rich SN was discovered, SN 2024ggi (T.-W. Chen et al. 2025), for which recent studies find a variable RSG progenitor (D. Xiang et al. 2024a). These objects provide a rare glimpse into the final properties of RSGs before their explosions.

Historically, few studies have attempted to follow the hydrodynamical evolution of stars before explosion (A. Heger et al. 1997; S.-C. Yoon & M. Cantiello 2010). M. Clayton et al. (2017) studied the hydrodynamical properties of giants with unstable envelopes self-consistently in the context of common-envelope evolution, and M. Clayton (2018) explored the properties of RSGs and their mass loss shortly before explosion. J. A. Goldberg et al. (2020) calculated the pulsations of a large range of massive stars. By introducing a velocity perturbation in the envelope, they triggered radial pulsation in stellar models of RSGs at the end of core carbon burning. J. A. Goldberg et al. (2020) revealed that such pulsations can affect the final structure of stars, their stellar LCs, and also their SN LCs. Following up on the work of M. Clayton et al. (2017, 2018), we recently computed the hydrodynamic evolution of a 15 $M_\odot$ RSG self-consistently (V. A. Bronner et al. 2025, hereafter Paper I) and found that it naturally undergoes pulsations through a $\kappa\gamma$-mechanism (A. Heger et al. 1997; S.-C. Yoon & M. Cantiello 2010; M. Clayton et al. 2017; A. Suzuki & T. Shigeyama 2025). We discussed the origin and mechanism behind the pulsations and showed that they strongly affect the pre-SN structure of the RSG, leading to SNe of varying SN LC decline rates that may be classified as Type II-P, short-plateau II-P, or Type II-L. In this Letter, we extend our study to multiple initial masses and show that large-amplitude pulsations can significantly change the pre-SN structure and explosion properties of RSGs. By comparing our models of pulsating RSGs to SNe with observed pulsating progenitors, we show that the observational characteristics of both the SN and pre-SN stellar LCs can be understood as the consequence of naturally occurring pulsations of RSGs. We demonstrate that HS models are insufficient to describe the structure of such stars and their explosions, and we emphasize the need for hydrodynamical models for understanding the final evolution and explosion properties of massive stars.

Our methods for the progenitor and explosion modeling are described in Sections 2.1 and 2.2, respectively. Following the same approach as in Paper I, we investigate the effect of pulsations on the final properties of massive single stars with different initial masses in Section 3.1. We explore the resulting SN LCs and photospheric velocities at different pulsation phases in Section 3.2. In Section 3.3, we check the claimed variability of the progenitors of SN 2024ggi and SN 2023ixf and demonstrate that there is no conclusive evidence for pulsations in SN 2024ggi. We then compare our models to the progenitor of SN 2023ixf in Section 3.4 and to its explosion properties in Section 3.5. We discuss our findings in Section 4 and present our conclusions in Section 5.

## 2. Methods

### 2.1. Modeling Red Supergiant Supernova Progenitors

We use the stellar evolution code MESA, v.10398 (B. Paxton et al. 2011, 2013, 2015, 2018, 2019), to simulate the evolution of massive single, nonrotating stars with initial masses of 10.5, 12.5, and 15.0 $M_\odot$ at solar metallicity ($Z = 0.0142$) until the onset of core collapse. Following the method described in Paper I, we compute the hydrodynamic evolution of these stars at the end of core carbon burning and follow the formation of stellar pulsations until they reach a steady and periodic equilibrium state. In particular, we use the implicit hydrodynamic solver, which makes use of artificial viscosity (for a discussion about the solver and implications of damping, see Appendix A of Paper I). The 15 $M_\odot$ model is described in detail in Paper I. For the 10.5 and 12.5 $M_\odot$ models we follow the same approach as in Paper I and remove the core at 3.6 and 2.8 $M_\odot$, respectively, corresponding to 90% for the helium core mass. An important factor for the pulsations is our choice for the efficiency of convection, which is computed according to mixing-length theory (MLT) with an efficiency parameter $\alpha_{\rm MLT} = 1.8$. We simulate the optical and infrared stellar LCs of these pulsating RSGs using MARCS models (B. Gustafsson et al. 2008) to describe the RSG spectrum and include a dust-shell model with the DUSTY code (Z. Ivezic & M. Elitzur 1997, 1999) for predicting the optical and infrared stellar LCs (for a detailed description, see Section 2.3 of Paper I).

### 2.2. Modeling Supernova Light Curves

By the end of the evolution of massive stars, strong neutrino losses decouple the rapidly evolving core from the envelope (e.g., S. E. Woosley et al. 2002). Core collapse may thus occur at any point during envelope pulsations. We compute the explosion of RSGs at different phases of the pulsation with the Lagrangian, one-dimensional hydrodynamical stellar explosion code SNEC, with the same assumptions as in Paper I. For our base assumptions of the explosion engine properties, we apply the semianalytical neutrino-driven SN code of B. Müller et al. (2016) with the same calibrations as in F. R. N. Schneider et al. (2021), D. Temaj et al. (2024), and E. Laplace et al. (2025), which results in a neutron star mass $M_{\rm NS}$, explosion energy $E$ (in units of bethe, $1\,{\rm B} = 10^{51}$ erg), and mass of synthesized $^{56}$Ni $M_{\rm Ni}$. For our default models, we assume that nickel is uniformly mixed throughout the stellar envelope until a boundary mass $M_b = 0.9M$, where $M$ is the final mass of the star. The explosion properties are summarized in Table 1 in Appendix A. Using publicly available data, we compare our models to SN 2024ggi and SN 2023ixf. To fit the SN data of SN 2023ixf, we construct 2016 SNEC models in which we vary the explosion properties ($E$ from 0.9 to 1.45 B, $M_{\rm Ni}$ from 0.05 to 0.06 $M_\odot$, $M_b$ from $0.5M$ to $0.99M$) for progenitors at different pulsation phases $\phi_{\rm exp}$ at the moment of explosion.

## 3. Results

### 3.1. RSG Pulsations for Different Initial Masses

Our models of RSGs experience radial pulsations after core helium burning driven by a $\kappa\gamma$-mechanism for a large ratio of luminosity to mass $L/M$ (Paper I). The resulting variations in luminosity and radius $R$ create a loop in the Hertzsprung–Russell diagram (HRD), shown in Figure 1. In general, the more massive the star, the larger are the variations in $R$, $L$, and effective temperature $T_{\rm eff}$; the larger is the pulsation amplitude; and the longer is its period (Table 2 in Appendix A). This is because, to first order, the pulsation period is expected to be proportional to the dynamical timescale $\tau_{\rm dyn}$ of the envelope,

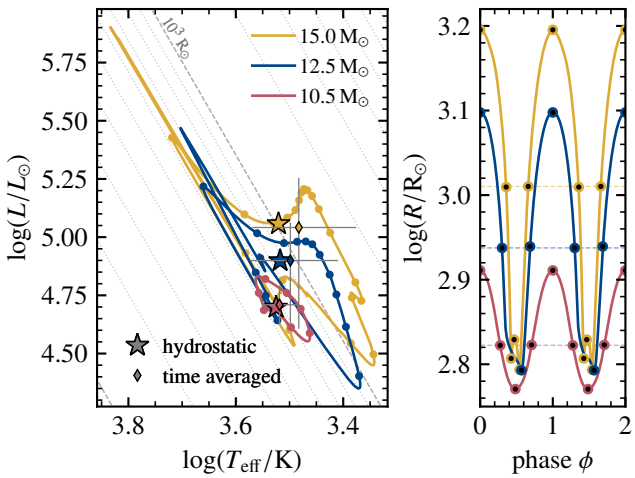


**Figure 1.** Final hydrodynamic evolution of stars with masses of 10.5, 12.5, and 15.0 $M_\odot$. Left: HRD of the pulsations. The initial HS models, as well as the time-averaged luminosity and effective temperature, are indicated. The markers along the pulsation tracks are spaced equally in time every 1/8, 1/15, and 1/20 of the pulsation period for the 10.5, 12.5, and 15.0 $M_\odot$ models, respectively. Right: radius evolution during the pulsations. The dashed horizontal lines show the radii of the HS models. Markers indicate the times during the pulsation cycle for which we show SN LCs. We define $\phi = 0$ at maximal radial extent.

given by

$$\tau_{\rm dyn} = \sqrt{\frac{R_{\rm max}^3}{GM_{\rm env}}}, \quad (1)$$

with $M_{\rm env}$ the mass of the hydrogen-rich envelope, $R_{\rm max}$ the maximum stellar radius during the pulsations, and $G$ the gravitational constant, which increases for higher initial masses. The obtained period is also proportional to the luminosity, leading to a characteristic PL relation for a fixed evolutionary state. We verify that our models are in good agreement with observationally inferred PL relations (see Appendix B).

The more massive models also show signs of substructure in the radius evolution and in the HRD track. These originate from the interaction of noncoherently pulsating layers in the envelope and are a result of the thermal restructuring that occurs in these models (Paper I). Nonsinusoidal LCs with additional substructure have been observed in many variable RSGs (e.g., VX Sgr; L. L. Kiss et al. 2006; Y. Ren et al. 2019; E. Christodoulou et al. 2025). Similar substructure can also occur in classical Cepheids (e.g., G. Bono et al. 2024). The 10.5 $M_\odot$ model pulsates coherently, producing an almost sinusoidal radius variation and a smooth ellipsoidal track in the HRD.

### 3.2. SN Light Curves and Photospheric Velocities as a Function of Initial Mass

We now characterize the explosion properties of the stellar models. As shown in Figure 2, for the higher-mass models, in which the stars experience higher-amplitude pulsations and therefore stronger changes to the outer stellar structure, there are also larger variations in the explosion properties. For the same explosion assumptions, the 15 $M_\odot$ model shows strong variations in the resulting bolometric SN LCs, ranging from Type II-L–like to Type II-P–like shapes (see Paper I for more details). For the lower-mass model, we find that the SN LCs vary less and all resemble Type II-P SNe. For larger radii, we observe an early excess emission feature in the SN LCs, which is reminiscent of the early emission feature observed in a large fraction of Type II SNe and often attributed to CSM (e.g., V. Morozova et al. 2018). In our models, the "early excess" feature arises naturally from the SN photosphere traveling through the extended envelope. The extended outer atmosphere at these pulsation phases may also act in addition to CSM to cause even larger early luminosity excess and have a similar effect on the early explosion properties, such as the lower photospheric velocities (T. Moriya et al. 2011). Thus, what is typically attributed to CSM may in fact be well explained by a low-density extended envelope (S. W. Falk & W. D. Arnett 1977).

We show the photospheric velocities of SNe at different pulsation phases in the bottom panels of Figure 2. Just as for the bolometric SN LC, a larger scatter in the photospheric velocity evolution is found for the higher-mass models. They are most visible at early times, where explosions of stars with larger radii lead to lower photospheric velocities.

For SNe with a plateau phase in their SN LCs, we observe that the photospheric velocities converge to similar values during the plateau (from 20 days) and follow a similar power-law trend. Comparing with the recent average observed trend of the photospheric velocity of 122 Type II SNe by C. P. Gutiérrez et al. (2017) that uses the absorption minimum of the Fe II $\lambda$6159 line, $v_{\rm FeII}$, as a proxy, we find a very good agreement for the lower-mass models (Figures 2(d) and 2(e)). Our 15 $M_\odot$ model has a higher velocity than the average observed trend, which reflects its higher energy for a similar final mass compared to the lower-mass models. A good agreement is also found with the power-law trend derived for the normalized photospheric velocities of Type II-P SNe by T. Faran et al. (2014b). This trend can be interpreted as a consequence of the phase during which recombination of the hydrogen envelope dominates. At this point, the photosphere follows the outer edge of the recombination zone (e.g., M. C. Bersten et al. 2011), which recedes at a similar rate, independently of the initial explosion.

The photospheric velocity evolution for the models with larger radii, which have short-plateau or Type II-L–like SN LCs, deviates from this trend. After reaching the peak, the velocity decreases more slowly than for the models at smaller radii and stays nearly constant for the models with the largest radii (see Figure 2(f)). Thus, the photospheric velocities at early times (up to about 30 days) have the potential to help distinguish between different progenitor structures and to break some of the degeneracies in the explosion properties. This is also the case for nonpulsating models (L. Dessart et al. 2010), though the photospheric velocities are expected to show smaller variations in these stars, and for a shorter amount of time (within the first 10 days, see also Appendix D). We emphasize that all the photospheric velocity trends described here are qualitative. SNEC is limited to a blackbody approximation (V. Morozova et al. 2015). Accurate predictions for the line velocities, in particular at early and late times during which nonthermal effects play a large role, require radiative transfer modeling (A. Kozyreva et al. 2020). In summary, we find that the observable explosion properties from massive stars that experience a significant restructuring of their envelope due to their hydrodynamic evolution are

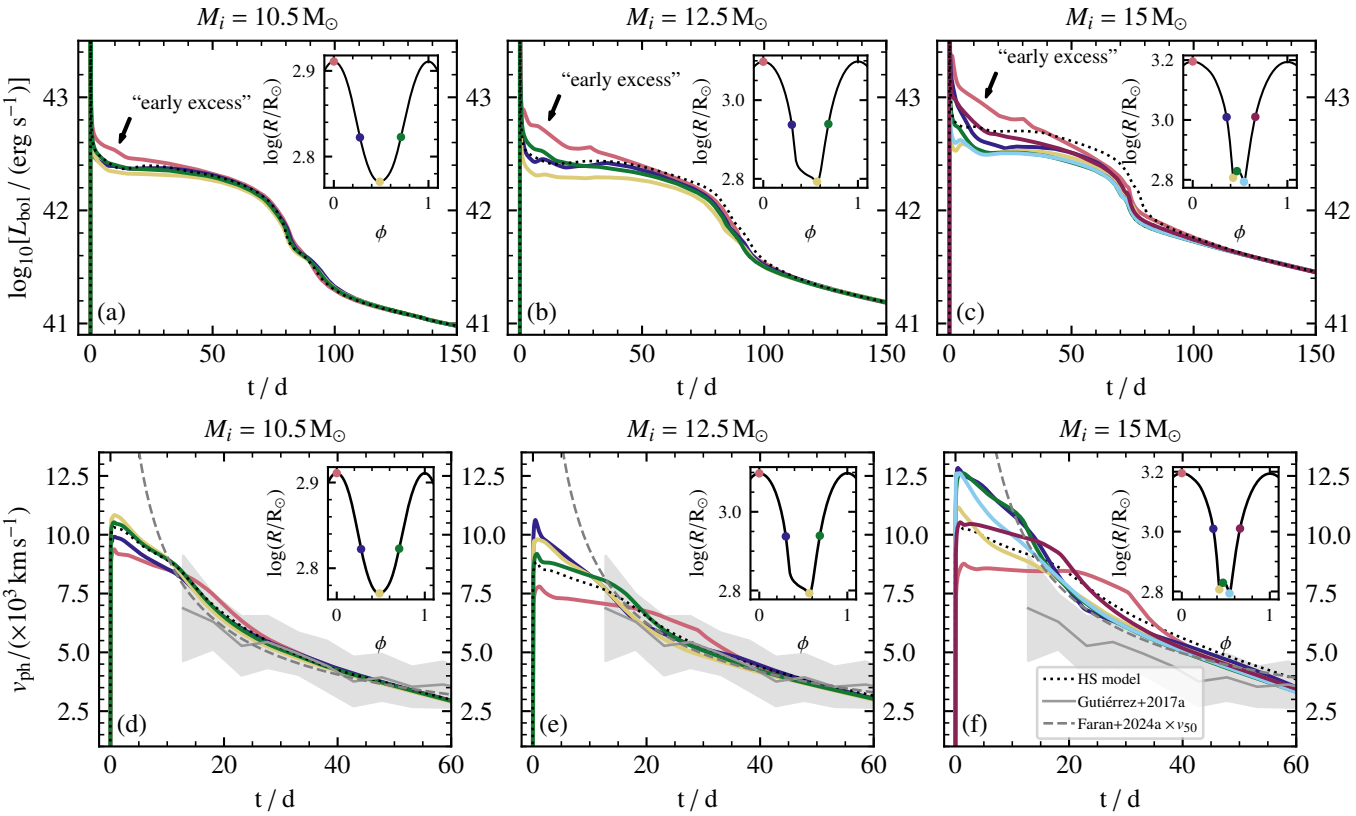


**Figure 2.** Explosion properties of pulsating RSG progenitors with different initial masses for varying explosion phases (indicated by different colors and highlighted in the insets) as a function of time after shock breakout. The dotted lines indicate the HS model. Top panels: bolometric SN LCs. Bottom panels: qualitative photospheric velocity evolution. The gray line shows the average relation inferred by C. P. Gutiérrez et al. (2017) for a sample of 122 observed Type II SNe, and the gray region indicates the $1\sigma$ standard deviation. For comparison, we additionally show the observationally inferred relation of T. Faran et al. (2014a) scaled by $v_{50}$, the velocity at day 50.

qualitatively different from those of the commonly assumed HS pre-SN models, as their envelopes have a significantly different structure (see also Appendix D for a more detailed comparison).

### 3.3. Verifying the Progenitor Variability of SN 2023ixf and SN 2024ggi

Before comparing our models to observational datasets of SNe with observed pulsating progenitors, we verify the reported progenitor variability of SN 20203ixf. Additionally, we do a periodicity study on the progenitor of SN 2024ggi, for which D. Xiang et al. (2024a) report periodic variability, therefore marking this SN as another potential test case with a pulsating progenitor.

For SN 2023ixf, J. E. Jencson et al. (2023) used archival pre-explosion data from the Spitzer Space Telescope to infer a period of $1119.4^{+132.4}_{-233.3}$ days. We take their photometric data and repeat their analysis using the Lomb–Scargle periodogram from the `astropy` Python package (Astropy Collaboration et al. 2013, 2018, 2022). We recover the reported period with two peaks in the periodogram at 975 and 1125 days and a full width at half-maximum of 360 days (Figure 3).

For SN 2024ggi, using archival pre-explosion images from the Hubble Space Telescope and the Spitzer Space Telescope, D. Xiang et al. (2024a) found a variable progenitor star with a period of $378.5 \pm 29.4$ days and attribute this to radial pulsations. Repeating their analysis, we recover the peak in the periodogram at a period of about 380 days, along with several other significant peaks at integer multiples of the base frequency (Figure 3). The base period found in the observational data from Spitzer is very close to that of the Spitzer spacecraft of ∼373.15 days (J. D. Giorgini & JPL Solar System Dynamics Group 1996). We do not find such a feature in the periodogram of the SN 2023ixf progenitor.

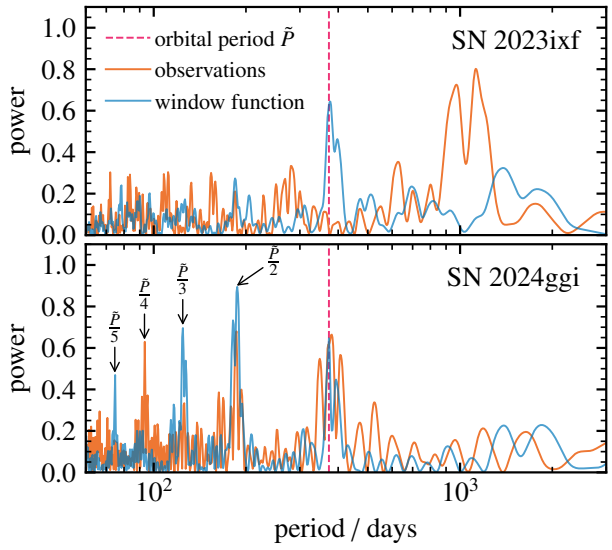


**Figure 3.** Lomb–Scargle periodogram of the progenitor observations of SN 2023ixf (J. E. Jencson et al. 2023) and SN 2024ggi (D. Xiang et al. 2024a). The window function of the observations, as well as the orbital period of the Spitzer spacecraft of $P = 373.15$ days, is shown as a comparison.

When computing the periodogram of the window function for SN 2024ggi, we find peaks at the same periods (Figure 3). The periodicity may therefore be a result of the periodic observation schedule. More detailed photometric analysis of the progenitor is consequently needed to conclusively identify the progenitor of SN 2024ggi as undergoing radial pulsations. This is beyond the scope of our modeling work. We therefore choose to exclude this object from further analysis.

Recent studies derive an initial mass of 10–15 $M_\odot$ for SN 2024ggi based on nebular spectroscopy (L. Dessart et al. 2025; L. Ferrari et al. 2025; E. Hueichapán et al. 2025), 10.5 $M_\odot$ from the environment close to the explosion site (X. Hong et al. 2024), and 13 $M_\odot$ via direct progenitor detection (D. Xiang et al. 2024b). As shown in Section 3.1, from our lower-mass models, we would expect that this progenitor is pulsating, probably mildly. The SN 2024ggi progenitor data are unfortunately inconclusive in our analysis. If no evidence for pulsations is found in the RSG progenitor, this would place interesting constraints on the $L/M$ range of the progenitor and also imply that its pre-explosion HRD location may actually be used to estimate its final core mass (D. Temaj et al. 2024). The unusually long plateau duration of SN 2024ggi (K. Ertini et al. 2025), which implies a large envelope mass, together with a small core mass, points to a likely merger or accretion product (F. R. N. Schneider et al. 2025).

In the following, we therefore only consider SN 2023ixf for our model comparison.

### 3.4. Model Comparison to the Progenitor Properties of SN 2023ixf

We now compare our models to the properties of SN 2023ixf, beginning with its RSG progenitor. Several independent studies have attempted to constrain the pre-SN $L$ and $T_{\rm eff}$ for SN 2023ixf based on the progenitor data (J. E. Jencson et al. 2023; C. D. Kilpatrick et al. 2023; Z. Niu et al. 2023; M. D. Soraisam et al. 2023; J. M. M. Neustadt et al. 2024; Y.-J. Qin et al. 2024; C. L. Ransome et al. 2024; S. D. Van Dyk et al. 2024; D. Xiang et al. 2024b). The derived values are shown in Figure 4, with the associated uncertainties. Despite being based on similar data, the derived $L$ and $T_{\rm eff}$ vary by up to 0.5 dex, and the inferred initial masses by a factor of 2 (J. E. Jencson et al. 2023; C. D. Kilpatrick et al. 2023; Y.-J. Qin et al. 2024; M. D. Soraisam et al. 2023; D. Xiang et al. 2024b).

These findings are based on observations from the Spitzer Space Telescope in Channel 1 (3.6 $\mu$m) and Channel 2 (4.5 $\mu$m), as well as ground-based near-infrared (NIR) observations in the $J$, $H$, and $K$ bands.

Comparing our model of a 15 $M_\odot$ pulsating RSG, shown by the solid line in Figure 4, to the inferred progenitor location, we find that the pulsation track in the HRD encloses most observationally derived values within the reported uncertainty ranges. The total spread is also of the same order as the time-averaged spread in $L$ and $T_{\rm eff}$ that we expect during one pulsation cycle.

Given that the studies that we compare to are mostly based on similar data, it appears that the systematic uncertainties are apparently much larger than the reported statistical uncertainties in $L$ and $T_{\rm eff}$ (see also B. Davies et al. 2013, 2018; E. R. Beasor et al. 2025). Different techniques for averaging the stellar LCs may contribute to the spread. Alternatively, the large spread could potentially be understood as a consequence

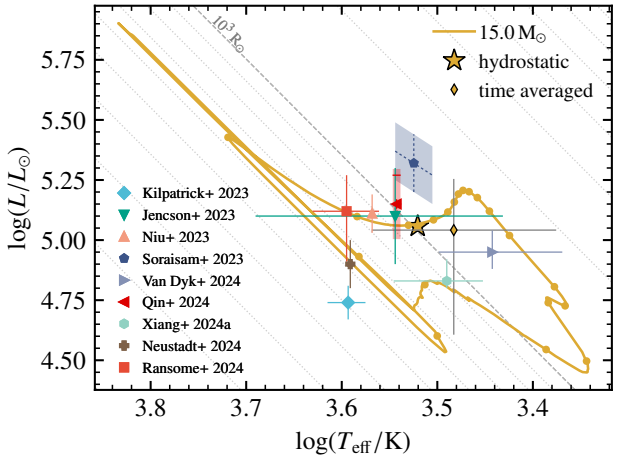


**Figure 4.** HRD of the 15 $M_\odot$ RSG model (solid line) during one pulsation cycle compared to observationally inferred pre-SN luminosities and temperatures of SN 2023ixf by different studies. Markers on the loop are spaced equally in time every 1/20 of the pulsation period. For reference, we show the location of the HS model. The time-averaged effective temperature and luminosity of our pulsating stellar model and the associated uncertainties are in good agreement with the spread in observationally inferred values. The shaded parallelogram indicates the possible progenitor location found by M. D. Soraisam et al. (2023). The reported luminosity spread due to the pulsations, reported by Y.-J. Qin et al. (2024), is shown as a vertical shaded bar, where the luminosity at the inferred explosion time is shown by the horizontal tick.

of different studies selecting various parts of the progenitor stellar LC to infer the pre-SN properties, which implies that they would be more sensitive to a certain pulsation phase. However, Y.-J. Qin et al. (2024) take the progenitor pulsations into account and find an amplitude of 0.13 dex in luminosity assuming a fixed $T_{\rm eff}$. Additionally, M. D. Soraisam et al. (2023) use a PL relation for their luminosity estimate. The example of SN 2023ixf thus shows that inferring core masses (let alone initial masses, which are affected by many more uncertainties, including mass loss, binary interactions, and mixing processes like overshooting; E. J. Farrell et al. 2020; F. R. N. Schneider et al. 2024, 2025; D. Temaj et al. 2024) of exploding RSGs from a single pre-SN $L$ and $T_{\rm eff}$ is not advisable for RSGs that experience high-amplitude pulsations before explosion.

An accurate measurement of the progenitor properties shortly before the explosion could constrain the pulsation phase during which the explosion occurred and help break some of the model degeneracies. In the case of SN 2023ixf, this phase is not well constrained, with the last Spitzer observations taken about 1300 days prior to explosion. There exist NIR observations within 200 days before explosion (J. E. Jencson et al. 2023; M. D. Soraisam et al. 2023). Unfortunately, the sparse coverage of the progenitor stellar LC in these filters prevents precise constraints on the pulsation phase at explosion.

We use DUSTY+MARCS models to derive the stellar LC of the 15 $M_\odot$ RSG,[9] with varying dust properties. In Figure 5, we fit this model to the observed stellar LC of the SN 2023ixf progenitor from J. E. Jencson et al. (2023; see Appendix C for the fitting procedure). The pulsation period of our default model (817 days) is lower compared to the inferred period between around 890 and 1250 days (see Figure 7 in

[9] The periods of the lower-mass RSG models are incompatible with the progenitor of SN 2023ixf.

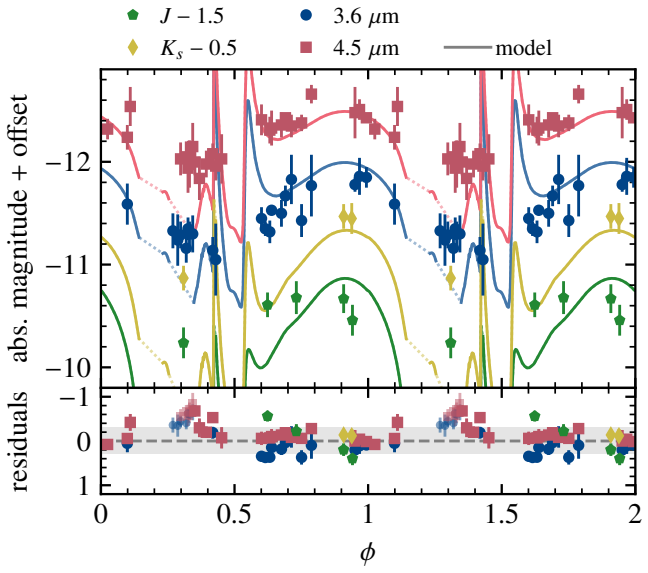


**Figure 5.** Phase-folded stellar LC of the 15 $M_\odot$ pulsating stellar model with a dusty envelope fitted to the observations of the SN 2023ixf progenitor from J. E. Jencson et al. (2023). For the stellar LC we assume silicate dust (V. Ossenkopf et al. 1992) with $\tau_0 = 13.5$, $P = 1120$ days, $\phi_{\rm exp} = 0.95$, and $T_{\rm in} = 1000$ K (see Figure 8 for full posterior distributions). The shaded–dotted sections of the stellar LCs are linear interpolations because the pulsation model lies outside the MARCS atmosphere model domain (see Appendix A in Paper I for a detailed discussion). The light residual points fall into the interpolated part of the stellar LC and are not considered in the fit.

Appendix B).[10] By rescaling the stellar LC accordingly (typically stretched by 10%–40%, depending on our assumptions for the dust properties; see Appendix C), we find a good agreement between the theoretical predictions and the observations of the SN 2023ixf progenitor. Note that we do not modify the amplitude or the baseline luminosity of the predicted stellar LC. The deviations between the model predictions and the observations are typically less than 0.3 mag, except for the observations around $\phi = 0.4$. Here the models predict brightness variation of $\sim$2 mag on timescales of a single day owing to ionization effects at the outer boundary. Whether such variations on these short timescales would manifest themselves in stars with a more advanced treatment of the atmosphere, as well as how these would interact with the dust envelope, is not clear. Therefore, we attribute less weight to this phase in the pulsation cycle and accept larger deviations between the models and the observations. The fits in the $J$ and $K_s$ bands also show larger deviation compared to the Spitzer band. This is caused by fewer data points in the filters.

The Spitzer data have coverage of only about 2.5 periods of the progenitor stellar LC (between 4200 and 1300 days before explosion) and do not cover the final year before explosion. This means that the uncertainty of the estimated period is larger than 10% (J. E. Jencson et al. 2023; C. D. Kilpatrick et al. 2023; M. D. Soraisam et al. 2023; D. Xiang et al. 2024b). Extrapolating the pulsations to accurately estimate the pulsation phase at explosion is impossible. This causes degeneracies between the fitting parameters of our theoretical model, such as the dust temperature at the inner boundary of the dust envelope or the dust composition, but also the pulsation phase at explosion (see Appendix C). Given these constraints, it is not possible to precisely determine the progenitor properties or the explosion phase $\phi_{\rm exp}$ from this dataset. Based on a Bayesian inference approach (see Appendix C), we find that values of $\phi_{\rm exp} \approx 0.9$–$0.4$, around the maximum radius, are favored (see Figure 8 in Appendix C). This underlines the importance of pre-explosion stellar LCs for understanding the progenitors of SNe and the last phases of their evolution.

### 3.5. Model Comparison to the Explosion Properties of SN 2023ixf

Given the overall good agreement between our 15 $M_\odot$ model and the SN 2023ixf progenitor properties, we focus on this model for inferring the explosion properties, implying a fixed ejecta mass of $M_{\rm ej} = 10.7$ $M_\odot$. We note that the 10%–40% uncertainty in the pulsation period of our model compared to the SN 2023ixf progenitor period (see Section 3.3) implies an underlying uncertainty in this ejecta mass after explosion. We construct 2016 SNEC models in which we vary the explosion properties ($E$ from 0.9 to 1.45 B, $M_{\rm Ni}$ from 0.05 to 0.06 $M_\odot$, $M_b$ from $0.5M$ to $0.99M$) for the range of explosion phases $\phi_{\rm exp}$ shown in Figure 2(c). The parameter space of explosion properties is affected by numerous well-known degeneracies that make it difficult to further constrain $\phi_{\rm exp}$ (L. Dessart & D. J. Hillier 2019; J. A. Goldberg et al. 2019; L. Martinez & M. C. Bersten 2019; J. A. Goldberg & L. Bildsten 2020; L. Dessart & W. V. Jacobson-Galán 2023; Q. Fang et al. 2025). For instance, both lower explosion energies and smaller pulsation amplitudes lead to lower explosion luminosities and longer plateau durations (see also Appendix D). Two example SN LCs and photospheric velocities based on progenitors at explosion phases with significantly different radii ($R_* = 1009\,R_\odot$ for $\phi_{\rm exp} = 0.36$ and $R_* = 643\,R_\odot$ for $\phi_{\rm exp} = 0.43$) and explosion energies ($E = 0.9$ B and $E = 1.45$ B, respectively) that fit the late-time (>25 days) dataset very well are shown in Figure 6. To obtain a good fit for the first part of the SN LC, an additional component is needed. This is supported independently by the spectral evolution of SN 2023ixf, which is consistent with interaction with CSM (e.g., W. V. Jacobson-Galán et al. 2023; J. E. Jencson et al. 2023; N. Smith et al. 2023; A. Singh et al. 2024; E. A. Zimmerman et al. 2024). We construct a CSM model following the approach of V. Morozova et al. (2018). The CSM is computed based on a steady-state wind-like density profile $\rho_{\rm CSM}$ with a velocity law of $\beta = 0$ (T. Moriya et al. 2011; T. J. Moriya et al. 2023):

$$\rho_{\rm CSM}(r) = \frac{\dot{M}}{4\pi v_w r^2}, \tag{2}$$

where $\dot{M}$ is the mass-loss rate, $v_w$ the wind velocity, and $R_{\rm ext}$ the radial extent of the CSM (T. Moriya et al. 2011; T. J. Moriya et al. 2023). Based on observational constraints, we set the terminal wind velocity to $v_{w,\rm inf} = 115$ kms$^{-1}$ (N. Smith et al. 2023). As shown in Figure 6, the data constraints are not sufficient to discriminate between different CSM models, explosion energies, or pulsation phases, as we obtain very good SN LC fits for two models with different CSM properties ($m_{\rm CSM} = 0.43$ $M_\odot$ for $\phi_{\rm exp} = 0.36$ and $m_{\rm CSM} = 0.23$ $M_\odot$ for $\phi_{\rm exp} = 0.43$, and a factor two difference in $R_{\rm ext}$). Measurements of photospheric velocities at earlier

[10] Based on this period, we would prefer a more massive progenitor model. However, these models encounter numerical difficulties.

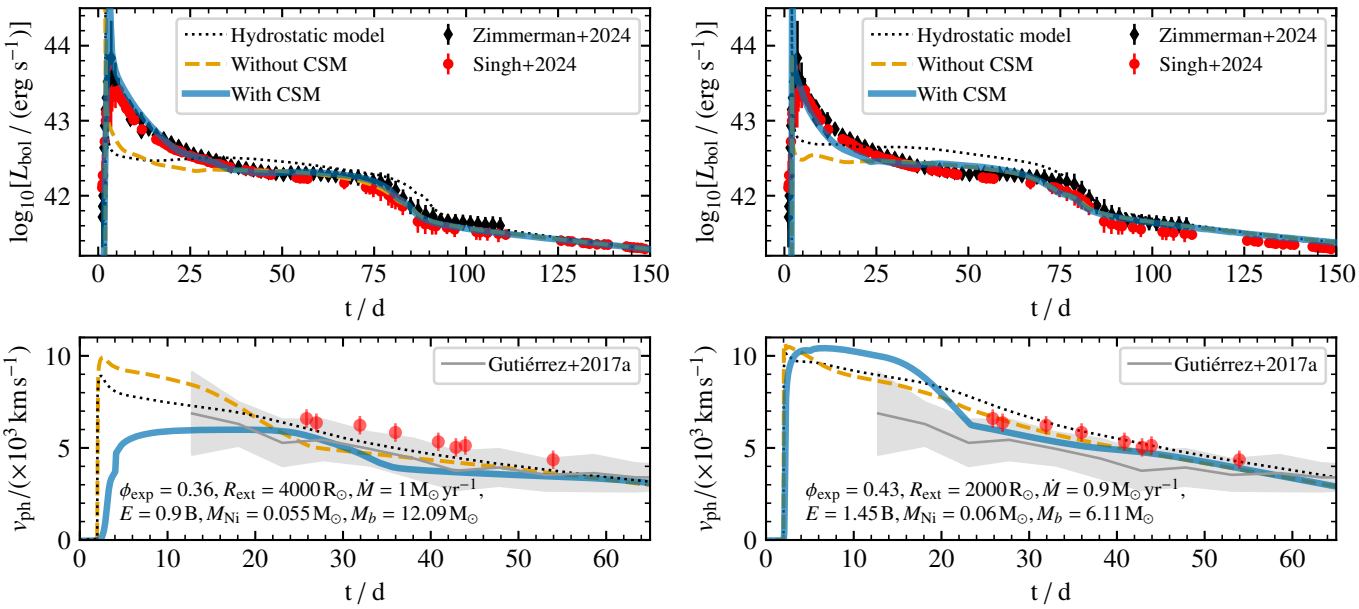


**Figure 6.** Two example SNEC explosion models based on the 15 $M_\odot$ RSG model with different radii / explosion phase and different explosion and CSM properties that both fit very well the observational data of SN 2023ixf. For comparison, the HS models with the same explosion properties without CSM are shown with dotted lines. Top: bolometric SN LC. Bottom: as a qualitative comparison, we show the predicted photospheric velocity evolution compared to the average $v_{\rm FeII}$ evolution of Type II SNe compiled by C. P. Gutiérrez et al. (2017).

times would provide clearer constraints. Given the blackbody approximation of SNEC, it is not the appropriate tool for deriving such constraints, which would require radiation transfer calculations.

Exploring a large range of SN explosion parameters (see above) and CSM properties ($\dot{M}$ from 0.2 to 0.9 $M_\odot\,{\rm yr}^{-1}$ and $R_{\rm ext}$ from 500 to 6000 $R_\odot$), we tentatively exclude explosions at maximum radial extent, as these result in rapidly declining SN LCs resembling Type II-L SNe that do not fit the SN LCs of SN 2023ixf well (see Figure 2). However, we do not find strong constraints on the explosion phase, given the large degeneracies in the SN properties and the presence of CSM.

In summary, combining our results for the pre-SN and explosion properties of SN 2023ixf, we find that our 15 $M_\odot$ fits the data very well. Our progenitor modeling favors a $\phi_{\rm exp}$ near radius maximum, but we do not find strong constraints from the SN LC modeling owing to underlying degeneracies. As pointed out by B. Hsu et al. (2024), the pulsation period of SN 2023ixf implies an independent constraint to the ejecta/envelope mass–radius–explosion energy relation obtained from the plateau phase of Type II SN LCs (D. V. Popov 1993; D. Kasen & S. E. Woosley 2009; J. A. Goldberg et al. 2019) and can therefore help break these degeneracies. The ejecta mass of $M_{\rm ej} = 10.7$ $M_\odot$ is in a similar range, but slightly higher than that obtained by several studies that performed modeling of the plateau based on HS models, where $M_{\rm ej} = 8$–$9.5$ $M_\odot$ (D. Hiramatsu et al. 2023; M. C. Bersten et al. 2024; B. Hsu et al. 2024; A. Singh et al. 2024; J. Vinko et al. 2025). However, as mentioned in Section 3.4, there is an underlying uncertainty in this ejecta mass due to the 10%–40% uncertainty in the pulsation period of the progenitor used to obtain this model. If $\phi_{\rm exp}$ (and therefore the pre-explosion radius) were to be better constrained, we could obtain a full solution for the explosion properties of SN 2023ixf.

## 4. Discussion

### 4.1. RSG Pulsations

The mass range at which radial RSG pulsations become important and significantly affect the pre-explosion structure sensitively depends on our assumptions regarding the envelope physics, in particular convection. In RSGs, both observations (e.g., M. Montargès et al. 2017) and expensive 3D modeling efforts (J. A. Goldberg et al. 2022; J.-Z. Ma et al. 2024) have shown that convection is an intrinsically 3D process, where large-scale convective cells easily break the spherical symmetry. Convection in these RSGs happens on similar timescales to the pulsations (Paper I), and it is unclear how exactly they will affect one another, but first modeling efforts find that these effects will probably be minor (G. E. Langer 1971; A. Heger et al. 1997). The latest 3D RSG models suggest that the fundamental radial mode dominates the pulsation (J.-Z. Ma et al. 2025), in line with observational expectations (e.g., L. L. Kiss et al. 2006; Y. Ren et al. 2019).

One-dimensional models typically simulate convection using MLT, where the efficiency is determined by the mixing-length parameter $\alpha_{\rm MLT}$. Its value is uncertain (M. Joyce et al. 2020), but recent 3D models of RSGs find that it may be in the range of $\alpha_{\rm MLT} \approx 1.4$–$3$ throughout the envelope (J. A. Goldberg et al. 2022; J.-Z. Ma et al. 2025). Observationally, this parameter is constrained by the observed radii of RSGs, which range from 400 to 1400 $R_\odot$ (B. Davies et al. 2013; M. Montargès et al. 2014; E. O'Gorman et al. 2015) and translate into a typical RSG location on the HRD. For example, S. Ekström et al. (2012) use $\alpha_{\rm MLT} = 1.6$ to fit observations by E. M. Levesque et al. (2005), while S.-H. Chun et al. (2018) find a metallicity-dependent $\alpha_{\rm MLT}$ value between 1.8 and 2.9. Recent Type II SN studies (based on HS stellar models) fit the color evolution better with smaller RSG radii of $\approx$500 $R_\odot$ (L. Dessart et al. 2013), corresponding to $\alpha_{\rm MLT} \approx 2.5$. Choosing a larger $\alpha_{\rm MLT}$ value, as in J. A. Goldberg et al. (2020), would shift the occurrence of

high-amplitude pulsations to higher-mass progenitors. We note that the use of MESA's MLT++ scheme in our models (see Paper I) reduces this apparent difference, as it leads to more compact RSGs.

In general, the periods obtained from the hydrodynamic modeling of the RSGs match the expectations from observational and theoretical PL relations (see Appendix B). The predicted amplitudes are, however, larger than observed amplitudes (e.g., Y. Ren et al. 2019). This can be explained by the observational bias toward core helium-burning RSGs, which are longer-lived than RSGs in more advanced burning phases. Additionally, simplified modeling of convection via MLT and its coupling to the pulsations can directly alter the modeled amplitudes, as well as the choice of the boundary conditions. For a more detailed discussion of these effects, see Section 5.4 in Paper I, but also M. Joyce et al. (2020) and A. Suzuki & T. Shigeyama (2025).

Another uncertain factor is the mass lost by the star before the explosion. If, for any reason, the star loses mass before explosion, the $L/M$ ratio will increase, and so will the pulsation amplitude. The effect described here may thus only apply to higher-mass RSGs or to stars that lose their envelopes before explosion, for example, due to binary mass transfer.

Since most massive stars live in interacting binaries (H. Sana et al. 2012), their pre-SN structures will be different compared to the single stars described here (P. Podsiadlowski et al. 1992; E. Laplace et al. 2021; F. R. N. Schneider et al. 2021, 2024), affecting the amplitude of RSG pulsations and the mass range at which they occur. For example, the signs of large-scale asymmetries in SN 2023ixf have been interpreted as signatures of past binary interactions (e.g., B. Hsu et al. 2024; A. Singh et al. 2024), which may imply more mass loss before explosion compared to single stars. We expect that not only donors in binary systems but also accretors and mergers may experience such pulsations, based on their pre-SN structures (F. R. N. Schneider et al. 2024, 2025). The interplay between envelope pulsations and binary interactions may further affect the pre-SN structure and is another uncertain and important aspect that we will study in the future.

### 4.2. Circumstellar Material

Our model does not self-consistently eject material owing to the pulsations. However, the development of subsurface shocks and the low binding energy at the phase of radius minimum (see Appendix A and Paper I) lead us to speculate that envelope ejections shortly before core collapse may be likely in pulsating SN progenitors (see also M. Clayton 2018), naturally producing the CSM observed in SN 2023ixf. Pulsation-driven mass ejections are expected for higher-mass progenitors (M. Clayton 2018), may explain the origin of this CSM (S.-C. Yoon & M. Cantiello 2010), and could be observed as SN precursors in case of particularly high mass ejections. Alternatively, the thermal restructuring phase we identify in our models for high-amplitude pulsation can also radiate away about $5 \times 10^{46}$ erg of energy over about 30 days (similar to observed luminous red novae; see Paper I) and could also be observed as an SN precursor. The existence of an SN precursor was recently proposed to explain the early explosion properties of SN 2023ixf (A. Kozyreva et al. 2025). Based on our model, it would be unlikely that such a precursor would be detected so shortly before explosion. Based on archival searches, no bright precursor is detected for SN 2023ixf in the past 5 yr before explosion (Y. Dong et al. 2023), which would disfavor a single episode of high mass ejection and would instead be consistent with mass loss over a long period of time, possibly due to pulsations.

From the pulsation period of the SN 2023ixf, we would expect a higher-mass progenitor than the one modeled here, which would be more likely to experience mass loss due to pulsations. Very recently, S. Sengupta et al. (2025) showed that the pulsation-driven mass loss, described following the prescriptions by S.-C. Yoon & M. Cantiello (2010) and M. Clayton (2018), can lead to significant mass loss in RSGs and explain the CSM structure of SN 2023ixf reasonably well. For higher-mass progenitors with stronger mass loss, this could lead to a runaway mass-loss process of pulsations with increased amplitude, triggering stronger mass ejections until the star has lost so much mass that it no longer appears as an RSG (Paper I). This may explain the lack of high-luminosity RSG SN progenitors (also known as the missing RSG problem; S. J. Smartt et al. 2009; S. J. Smartt 2015). We emphasize that not all signatures of CSM in SN explosions are necessarily connected to pre-SN mass loss. Instead, "early excess" features identified in a large fraction of Type II SN LCs can alternatively be explained by extended progenitors (e.g., S. W. Falk & W. D. Arnett 1977; A. Ercolino et al. 2024). Here we show that radial pulsations, in particular in high-mass RSGs, can naturally lead to extended SN progenitors. We predict that these signatures should be more prevalent in SNe from progenitors that experience higher-amplitude pulsations. Recently, J. Fuller & D. Tsuna (2024) discussed the effect of RSG chromospheres on SN LCs and showed that these can translate into early luminosity excess. Taking these chromospheres or, similarly, "effervescent zones" that may be created by a combination of pulsation-driven outflows and convection in the envelope (N. Soker 2021, 2023) into account for our pulsating progenitors would thus further enhance the early emission we described. We expect that, together with radial pulsations, this could also help explain the prevalence of early "flash ionization" signatures in Type II SNe (R. J. Bruch et al. 2021) and their long rise time until shock breakout (F. Förster et al. 2018), without the need of invoking unknown pre-SN mass-loss processes. Recently reported observations show that Type II SNe with early ionization signatures have typically luminous fast-declining SN LCs (W. V. Jacobson-Galán et al. 2025). This is consistent with high-mass stars preferentially exploding with large radii owing to pulsations (Paper I). Pulsations can also explain the 0.2 dex spread between the $i$-band and spectral energy distribution luminosities in observed RSGs (E. R. Beasor et al. 2025).

## 5. Conclusion

We investigate the pre-SN evolution of massive RSGs between 10.5 and 15 $M_{\odot}$, focusing on their hydrodynamical evolution and the effect on their explosion properties. In line with previous studies (A. Heger et al. 1997; S.-C. Yoon & M. Cantiello 2010; M. Clayton 2018; J. A. Goldberg et al. 2020), we find that they all develop radial envelope pulsations. In our more massive progenitors, the pulsations lead to a restructuring of the envelope that leads to a significantly different pre-SN envelope structure compared to HS models. We show that pulsations significantly affect the pre-SN properties of RSGs, including their location on the HRD, and that their importance increases with mass. Based on our

findings, we caution against inferring core masses (let alone initial masses) for massive pulsating RSGs from a single pre-SN HRD location.

Studying the explosion properties of these pulsating RSGs, we show that the changing structure as a function of pulsation phase can lead to significant variations compared to HS progenitors. In particular, extended progenitors appear to have an "early excess" in their SN LCs, even for our low-mass progenitors. This early excess is observed in a large fraction of SNe (up to 60%; V. Morozova et al. 2018) and is often attributed to CSM of unknown origin (V. Morozova et al. 2018; K. R. Hinds et al. 2025). Here we show that it can at least in part be the result of a more extended progenitor structure due to radial pulsations, and it could potentially be extended further if chromospheres of RSGs were taken into account (J. Fuller & D. Tsuna 2024). This same effect could also provide a natural explanation for "flash ionization" signatures in the spectra of a large fraction of Type II SNe (R. J. Bruch et al. 2021), which are preferentially found in luminous SNe with fast-declining SN LCs (W. V. Jacobson-Galán et al. 2025). Analytical scaling relations typically used for inferring SN properties (D. V. Popov 1993; D. Kasen & S. E. Woosley 2009; J. A. Goldberg et al. 2019) should therefore be used with caution, in particular for luminous SNe with early excess (see Appendix D).

As a function of the pulsation phase, we find significant variations in the photospheric velocity evolution, in particular at early times (before 25 days), whose importance increases for higher-mass progenitors that experience larger-amplitude pulsations. These features can help break long-standing degeneracies (D. Kasen & S. E. Woosley 2009; J. A. Goldberg et al. 2019) in the explosion properties of Type II SNe.

We apply our models to the recent SN 2023ixf and SN 2024ggi, for which pulsating RSG progenitors were reported. We find insufficient evidence for the claimed pulsation period of the SN 2024ggi progenitor, as it matches Spitzer's orbital period. Based on its explosion properties, we speculate that it may be a binary stellar merger product.

We recover the reported pulsation period of SN 2023ixf and demonstrate that the pre- and post-explosion characteristics can all be fit very well with our exploding pulsating RSG models. However, the data coverage is insufficient to break the degeneracies in explosion parameters and pulsation phase. Based on the good agreement between our model and the pre-SN and explosion parameters, we tentatively constrain the explosion phase to be at intermediate pulsation radii. If it were precisely determined, we could find a full solution for the explosion properties of SN 2023ixf. This shows the large potential of leveraging pulsating progenitors for constraining SN properties and underlines the limitation of HS models. We speculate that the CSM in SN 2023ixf is also connected to pulsations through pulsation-driven outflows (S.-C. Yoon & M. Cantiello 2010; M. Clayton 2018; S. Sengupta et al. 2025). Such outflows are expected to be more prevalent in higher-mass progenitors owing to the dependence of the $\kappa\gamma$-mechanism on the $L/M$ ratio (Paper I).

The exact mass range in which pulsations play an increased role for the pre-SN structure is subject to large uncertainties regarding the mixing processes in stars, their mass loss, and their binary interactions (see also Paper I). However, in any case, we expect that RSGs on the more massive end experience large-amplitude radial pulsations shortly before their explosion.

This study emphasizes the importance of the hydrodynamic evolution of stars, in particular from $\sim$15 $M_\odot$, for their last evolutionary stages, their pre-SN, and explosion properties. With the start of next-generation all-sky surveys such as the Legacy Survey of Space and Time of the Vera Rubin Telescope, it will become easier to detect SNe with variable progenitors, giving us more opportunities to further understand the importance and prevalence of pulsations in SN progenitors.

## Acknowledgments

We thank the anonymous referee for their thorough review, which helped improve this work. We thank Avinash Singh and Brian Hsu for generously providing early datasets of SN 2023ixf. We also thank Takashi Moriya, Jared Golberg, Ebraheem Farag, and Emma Beasor for constructive discussion that helped improve this work. V.A.B., E.L., F.R.N.S., and P.P. acknowledge support from the Klaus Tschira Foundation. This work has received funding from the European Research Council (ERC) under the European Union's Horizon 2020 research and innovation program (grant agreement No. 945806) and is supported by the Deutsche Forschungsgemeinschaft (DFG, German Research Foundation) under Germany's Excellence Strategy EXC 2181/1-390900948 (the Heidelberg STRUCTURES Excellence Cluster). V.A.B. acknowledges support from the International Max Planck Research School for Astronomy and Cosmic Physics at the University of Heidelberg (IMPRS-HD). E.L. acknowledges support through a start-up grant from the Internal Funds KU Leuven (STG/24/073) and through a Veni grant (VI. Veni.232.205) from the Netherlands Organization for Scientific Research (NWO). This research was supported by the Munich Institute for Astro-, Particle and BioPhysics (MIAPbP), which is funded by the Deutsche Forschungsgemeinschaft (DFG, German Research Foundation) under Germany's Excellence Strategy EXC-2094–390783311.

*Software:* Astropy (Astropy Collaboration et al. 2013, 2018, 2022), CMasher (E. van der Velden 2020), Matplotlib (J. D. Hunter 2007), NumPy, (C. R. Harris et al. 2020), PyAstronomy (S. Czesla et al. 1906), PYPHOT (M. Fouesneau 2025), SciPy (P. Virtanen et al. 2020).

## Appendix A
## Additional Model Properties

For reference, we show additional properties of our models in Tables 1 and 2. The assumed explosion parameters for our default SNEC models are obtained through the semianalytical neutrino-driven explosion code of B. Müller et al. (2016), with calibrations as in F. R. N. Schneider et al. (2021), D. Temaj et al. (2024), and E. Laplace et al. (2025).

**Table 1**
Summary of the Explosion Properties of the RSG Models with Different Initial Mass $M_i$

| $M_i$ ($M_\odot$) | $E$ ($10^{51}$ erg) | $M_{NS}$ ($M_\odot$) | $M_{Ni}$ ($M_\odot$) | $M_b$ ($M_\odot$) |
|---|---|---|---|---|
| 10.5 | 0.916 | 1.387 | 0.0295 | 8.70 |
| 12.5 | 0.871 | 1.597 | 0.0450 | 9.88 |
| 15.0 | 1.60 | 1.502 | 0.0863 | 11.0 |

**Note.** The explosion parameters are determined with the B. Müller et al. (2016) model, with calibrations as in F. R. N. Schneider et al. (2021).

**Table 2**
Summary of the Pulsation Properties of the RSG Models with Different Initial Mass $M_i$ and $L/M$ (in Solar Units)

| $M_i$ ($M_\odot$) | $\log(L/M)$ | $P_{\rm GY\ RE}$ (days) | $P_{\rm growth}$ (days) | $P$ (days) | $\Delta \log R$ (dex) | $\Delta \log L$ (dex) | $\Delta \log T_{\rm eff}$ (dex) | $M_{\rm env}$ ($M_\odot$) | $P/\tau_{\rm dyn}$ | $\left(\frac{v_{\rm surf}}{v_{\rm esc}}\right)_{\rm max}$ | $\phi_{v_{\rm surf,max}}$ |
|---|---|---|---|---|---|---|---|---|---|---|---|
| 10.5 | 3.71 | 470 | $477^{+13}_{-15}$ | $490^{+5}_{-7}$ | 0.14 | 0.28 | 0.10 | 6.56 | 2.92 | 0.180 | 0.76 |
| 12.5 | 3.86 | 745 | $740^{+40}_{-40}$ | $702^{+8}_{-7}$ | 0.31 | 1.12 | 0.33 | 6.97 | 2.27 | 0.430 | 0.67 |
| 15.0 | 3.91 | 1010 | $920^{+110}_{-70}$ | $817^{+8}_{-11}$ | 0.40 | 1.45 | 0.49 | 6.99 | 1.86 | 0.507 | 0.62 |

**Note.** We show peak-to-peak amplitudes of the radius $R$, luminosity $L$, and effective temperature $T_{\rm eff}$; the pulsation period in units of the dynamical timescale (Equation (1)); the maximum of the surface velocity $v_{\rm surf}$ over the escape velocity $v_{\rm esc}$, with $v_{\rm esc} = (2GM/R)^{1/2}$; and the corresponding pulsation phase.

We summarize the pulsation properties of the model in Table 2. With increasing mass, the amplitudes in the stellar radius $R$, luminosity $L$, and effective temperature $T_{\rm eff}$ become larger. To first order, the pulsation period scales linearly with the dynamical timescale $\tau_{\rm dyn}$ of the model. We find that the ratio of surface velocity and escape velocity $v_{\rm surf}/v_{\rm esc}$ also increases with mass. This is expected because the pulsations become stronger for larger $L/M$. For $v_{\rm surf}/v_{\rm esc} > 1$, we would expect dynamical mass ejection. This agrees with the results in M. Clayton (2018), where dynamical mass ejections only occur for $\log(\frac{L/L_\odot}{M/M_\odot}) > 4.1$. We expect the mass ejection to happen typically shortly after maximum compression (around $\phi \sim 0.65$), where $v_{\rm surf}/v_{\rm esc}$ reaches its maximum value (see also M. Clayton et al. 2017 and M. Clayton 2018).

We use GYRE (R. H. D. Townsend & S. A. Teitler 2013) to determine the period of the fundamental radial mode, $P_{\rm GY\ RE}$, based on the initial HS models (see also M. Joyce et al. 2020). Additionally, we computed the pulsation period, $P_{\rm growth}$, during the exponentially growing phase of the pulsations (see Section 3.1 in Paper I). We find that $P_{\rm GY\ RE}$ and $P_{\rm growth}$ are compatible within the uncertainties, but the period $P$ of the steady-state pulsation deviates. This is expected because, after the initial transient phase and potentially a catastrophic cooling event, the envelope structure changes, and therefore its dynamical properties also change. This also means that it is not possible to accurately determine the pulsation period using a perturbation analysis of the initial HS model.

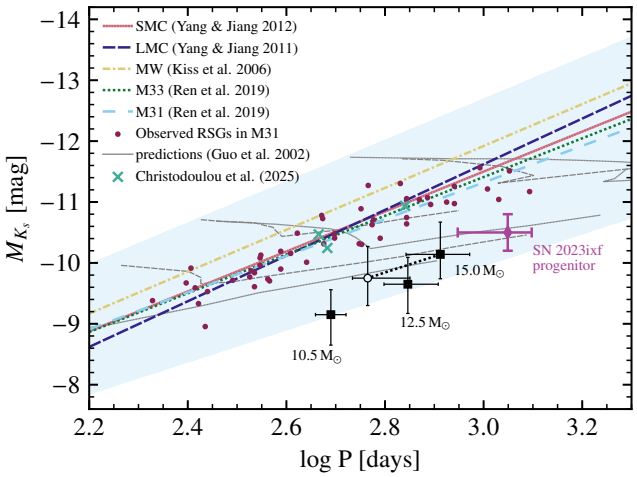


**Figure 7.** Comparing models of pulsating RSGs to observationally determined PL relations in various environments (L. L. Kiss et al. 2006; M. Yang & B. W. Jiang 2011, 2012; Y. Ren et al. 2019). The shaded region shows the uncertainty of the PL relation for M31 and is characteristic for all the others. Theoretical predictions are from J. H. Guo & Y. Li (2002) for evolving 15, 20, and 30 $M_\odot$ RSGs at $Z = 0.02$ and 0.01 (solid and dashed lines, respectively), adjusted with bolometric corrections from E. Josselin et al. (2000). For comparison, we show the recent observations from E. Christodoulou et al. (2025). The SN 2023ixf progenitor is taken from J. E. Jencson et al. (2023). The model with an open symbol connected to the 15 $M_\odot$ RSG is taken at the end of core helium burning.

## Appendix B
## Comparison to Observed and Predicted PL Relations of RSGs

We compare the periods of the steady-state pulsations obtained from our RSG models with observationally determined PL relations recovered in various environments (Figure 7). For our three RSG models, the uncertainty the pulsation periods is determined by using the same sampling as in the Spitzer observations of the SN 2023ixf progenitor. The uncertainty of the $K_s$-band magnitude takes into account different dust properties of the DUSTY radiation transfer models. As shown in Figure 7, there is a general trend of our models being located below the observational PL relations from large samples of RSGs. This is expected from theoretical predictions (solid and dashed black lines in Figure 7), as RSGs generally evolve to higher luminosities and longer pulsation periods at later evolutionary stages. In particular, the prediction for a $Z = 0.02$, 15 $M_\odot$ star close to core collapse is very close to our 15 $M_\odot$ RSG model (black point), for which we also find a similar evolution compared to its pulsation period at the end of core He burning (see the open symbol and dotted line in Figure 7). Observational samples of RSGs are dominated by stars in their long-lived core-He-burning phase and are thus located around shorter base periods. The observed periods of the progenitor of SN 2023ixf (purple point on Figure 7) cover a wide range, from around 890 to 1250 days. The observation is consistent with the trend in our models by having a long base period and high luminosity for an evolved star. The location on the PL diagram is compatible with our 15 $M_\odot$ model. In summary, we verify that our models are compatible with both observationally inferred and theoretically predicted PL relations for RSGs.

## Appendix C
## Fitting Progenitor Light Curve of SN 2023ixf

The progenitor stellar LCs are computed based on MARCS atmosphere models (B. Gustafsson et al. 2008) with the DUSTY radiation transfer code (Z. Ivezic & M. Elitzur 1997, 1999) and depend on the total optical depth $\tau_0$ (see Section 2.3 in Paper I). We consider three different dust compositions: warm silicates based on V. Ossenkopf et al. (1992), silicates based on B. T. Draine & H. M. Lee (1984), and graphite based on B. T. Draine & H. M. Lee (1984). The dust temperature at

the inner boundary $T_{\rm in}$ is varied between 800, 1000, and 1200 K. The computed stellar LCs are stretched and shifted to match any pulsation period $P$ and pulsation phase at explosion $\phi_{\rm exp}$.

We use a Bayesian inference approach to fit the progenitor stellar LC to the observed data collected in J. E. Jencson et al. (2023), with inferred quantities $\vec{\theta} = (\tau_0, P, \phi_{\rm exp})$. We choose a uniform prior for $\tau_0$ with bounds between 0.5 and 25. The prior for the pulsation period is proportional to the Lomb–Scargle power (Figure 3), bounded between 500 and 1500 days. The explosion phase $\phi_{\rm exp}$ is treated as a circular variable with a uniform prior between 0 and 1. To compare our model to the data, we choose a Gaussian likelihood function,

$$\ln\mathcal{L}(\boldsymbol{\theta}) = -\frac{1}{2}\sum_{i}^{N_{\rm obs}}\left[\frac{(m(\boldsymbol{\theta}, t_i) - m_{{\rm obs},i})^2}{s_i^2} + \ln(2\pi s_i^2)\right], \quad \text{(C1)}$$

where $m(\boldsymbol{\theta}, t)$ is the modeled magnitude at time $t$, $m_{{\rm obs},i}$ is the observed magnitude at time $t_i$, $s_i^2 = \sigma_i^2 + f^2 m(\boldsymbol{\theta}, t_i)$, and $\sigma_i$ is the observational uncertainty. The variable $f$ accounts for underestimated uncertainties of the posterior distribution, and we treat it as another inference quantity with a log-uniform prior (D. W. Hogg et al. 2010). Some data of J. E. Jencson et al. (2023) have very low uncertainties ($\sim$0.04 mag). We set an additional lower limit of 0.1 mag to the uncertainties to avoid underestimating the errors. The likelihood function sums all observations $N_{\rm obs}$ in $J$ band, $K_s$ band, Spitzer channel 1 (3.6 $\mu$m), and Spitzer channel 2 (4.5 $\mu$m) reported in J. E. Jencson et al. (2023). If an observation falls into the phase range where the stellar LC cannot be predicted, this observation is not taken into account. We sample from the posterior distribution using the `emcee` Python package (D. Foreman-Mackey et al. 2013), which is an implementation of the affine-invariant Markov Chain Monte Carlo ensemble sampler from J. Goodman & J. Weare (2010).

The marginalized posterior distributions for $\tau_0$, $P$, and $\phi_{\rm exp}$ are shown in Figure 8, where we have integrated over all values of $T_{\rm in}$ for a given dust composition. The dust composition directly sets the mode of the $\tau_0$-distribution, where graphite dust requires the lowest values ($\tau_0 \sim 4$) and silicates require the highest values ($\tau_0 \sim 14$–$20$). The dust composition has only a small impact on the posterior distribution of the period $P$. This is expected because the period prior, which is based on the Lomb–Scargle power, is already very informative and uses the observed data. In a Bayesian view, the power can also be seen as the posterior distribution when fitting a sinusoidal model to the data (E. T. Jaynes 1987). The posterior of the explosion phase $\phi_{\rm exp}$ shows a larger dependence on the dust composition. Taking all dust compositions into account, we find that $\phi_{\rm exp}$ can be constrained between 0.9 and 0.4, i.e., around the maximum radius of the progenitor. This phase is much longer-lived than the compressed phase because of a longer dynamical timescale (see Figure 1).

We show a corner plot of the posterior distribution for graphite-based dust (grdDL) in Figure 9. There is a clear correlation between the inferred pulsation period $P$ and the pulsation phase at explosion $\phi_{\rm exp}$. Nonetheless, there is a clear gap in the $\phi_{\rm exp}$ distributions around 0.5.

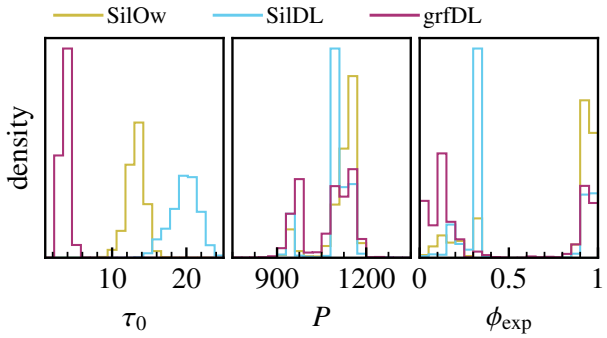


**Figure 8.** Posterior distributions of the optical depth $\tau_0$, the pulsation period $P$, and the pulsation phase at explosion $\phi_{\rm exp}$. Posteriors are shown for the different dust compositions: warm silicates based on V. Ossenkopf et al. (1992; SilOw), silicates based on B. T. Draine & H. M. Lee (1984; SilDL), and graphite based on B. T. Draine & H. M. Lee (1984; grfDL). The posteriors are summed over all three possible values for $T_{\rm in}$.

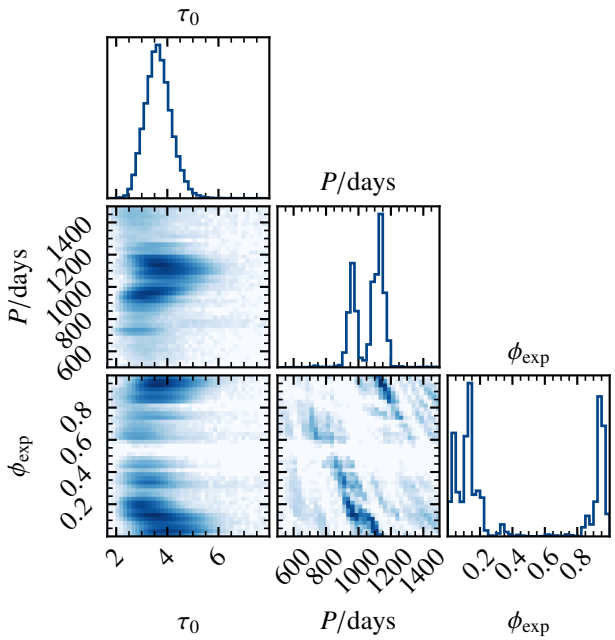


**Figure 9.** Corner plot showing the posterior distribution assuming graphite dust (B. T. Draine & H. M. Lee 1984). The 1D histograms use a linear ordinate, while the 2D histograms use a logarithmic scale on the coloring.

## Appendix D
## Comparison of SN Light Curves from Hydrostatic and Hydrodynamic Progenitors

Here we investigate the difference in the SN properties obtained between our approach of modeling the hydrodynamical pre-SN evolution of RSGs and the simple expectation of HS models used to derive analytical scaling relations to infer the properties of SNe, such as derived by D. V. Popov (1993), D. Kasen & S. E. Woosley (2009), and J. A. Goldberg et al. (2020).

To this end, we use analytical homology relations and compute pre-SN stellar properties based on the HS 15 $M_\odot$ pre-SN model with radius $R_{\rm HS}$ and radial coordinate $r_{\rm HS}$. For each pulsation phase / radius $R_2$ shown in Figure 2(c), we compute a new envelope structure. From the base of the envelope to the

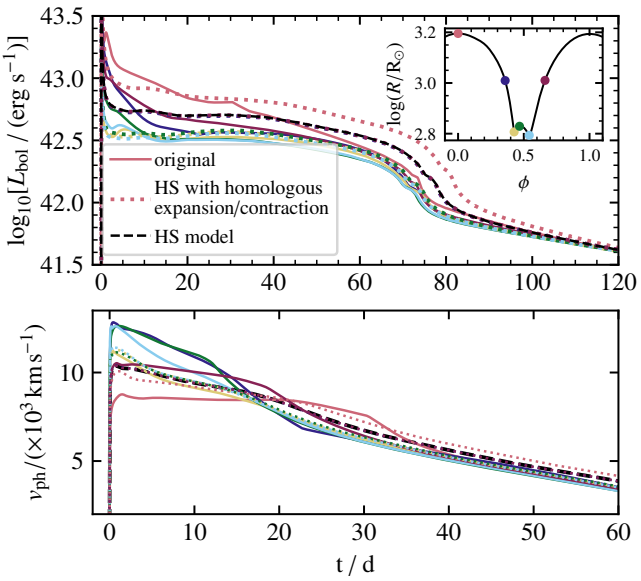


**Figure 10.** SN LC (top) and photospheric velocity evolution (bottom) of the 15 $M_\odot$ stellar model. Here we compare the explosion outcome of the hydrodynamic pre-SN model to the HS pre-SN model and to pre-SN models that assume homologous contraction/expansion of the HS model to the same radius as the one reached by the hydrodynamic model for different pulsation phases shown in the inset. All models have the same explosion energy, ejecta mass, and mass and distribution of $^{56}$Ni.

surface, we compute new pre-SN structures by computing homology relations for the local radial coordinate $r_2$, density $\rho_2$, and temperature $T_2$ in every layer, applying an adiabatic ideal gas equation of state, which is a good first approximation for the convective envelope of an HS RSG (e.g., R. Kippenhahn et al. 2013), such that

$$r_2 = r_{\rm HS}\frac{R_2}{R_{\rm HS}},\ \rho_2 = \rho_{\rm HS}\left(\frac{R_2}{R_{\rm HS}}\right)^{-3},\ \text{and}\ T_2 = T_{\rm HS}\left(\frac{R_2}{R_{\rm HS}}\right)^{-2}.$$

Based on these homologously expanded/contracted models, we then compute the SN LC with SNEC. As the core properties are unchanged, the explosion properties are also assumed to remain the same, and we apply the same explosion parameters obtained from the B. Müller et al. (2016) model as for Figure 2(c) (see Table 1).

As shown in Figure 10, the restructuring of the envelope in the hydrodynamic models (solid lines) indeed leads to a significantly different SN LC shape and photospheric velocity evolution compared to the homologously rescaled models (dotted lines). The same trend of increased SN luminosity for more extended models is recovered, but the scaled HS models all conserve their distinct Type II-P–like shape, and the more extended models have a longer plateau duration. In contrast, the SN LCs of the hydrodynamic models show significantly different shapes, ranging from Type II-L–like to Type II-P–like shapes. Interestingly, the time of the transition to the radioactive tail appears to be very similar for all hydrodynamical models, at about 75 days. Besides, no features are observed in the SN LCs of the rescaled HS models in Figure 10, as the SN progenitors do not exhibit the density inversions found in the hydrodynamic model caused by layers moving inward and outward owing to the $\kappa\gamma$-mechanism (see also Paper I for a detailed discussion of this phenomenon). Besides, the "early excess" identified in Figure 2 is not visible in the rescaled HS models. However, for the smallest radii, the SN LCs of the hydrodynamic and rescaled HS models are very similar and resemble a classical Type II-P–like shape, except at very early times (less than 5 days). For these models, the plateau duration and luminosity are all very similar.

Similarly, the photospheric velocity evolution is also systematically different for the scaled HS pre-SN structures compared to the the hydrodynamic pre-SN models, as shown in the bottom panel of Figure 10, especially for the more extended progenitors, which differ by a factor of up to two in the first 10 days. The photospheric velocities of the scaled HS model are all very similar and closely follow the trend of the initial HS model, as expected. Observing the early photospheric velocity evolution therefore provides a particularly strong constraint on the pre-SN structure of RSGs that experience a restructuring of their envelopes owing to envelope pulsations.

As analytical scaling relations of SN LCs are all based on the assumption of an HS progenitor star (D. V. Popov 1993; D. Kasen & S. E. Woosley 2009; J. A. Goldberg et al. 2019), applying these to SNe that experience a restructuring of their envelope owing to pulsations is therefore inadvisable. For example, if the most extended progenitor in Figure 10 were interpreted as a short-plateau II-P, one would find up to about 60% difference in plateau duration. In summary, this comparison emphasizes the importance of hydrodynamic pre-SN models to capture the full diversity of SN LCs and photospheric velocity evolutions from exploding RSGs.

## ORCID iDs

Eva Laplace https://orcid.org/0000-0003-1009-5691
Vincent A. Bronner https://orcid.org/0000-0002-7624-2933
Fabian R. N. Schneider https://orcid.org/0000-0002-5965-1022
Philipp Podsiadlowski https://orcid.org/0000-0002-8338-9677

## References

Antoniadis, K., Bonanos, A. Z., de Wit, S., et al. 2024, A&A, 686, A88
Astropy Collaboration, Price-Whelan, A. M., Lim, P. L., et al. 2022, ApJ, 935, 167
Astropy Collaboration, Price-Whelan, A. M., Sipőcz, B. M., et al. 2018, AJ, 156, 123
Astropy Collaboration, Robitaille, T. P., Tollerud, E. J., et al. 2013, A&A, 558, A33
Beasor, E. R., Davies, B., Smith, N., et al. 2020, MNRAS, 492, 5994
Beasor, E. R., Smith, N., & Jencson, J. E. 2025, ApJ, 979, 117
Bersten, M. C., Benvenuto, O., & Hamuy, M. 2011, ApJ, 729, 61
Bersten, M. C., Orellana, M., Folatelli, G., et al. 2024, A&A, 681, L18
Bono, G., Braga, V. F., & Pietrinferni, A. 2024, A&ARv, 32, 4
Bronner, V. A., Laplace, E., Schneider, F. R. N., & Podsiadlowski, P. 2025, A&A, 703, A61
Bruch, R. J., Gal-Yam, A., Schulze, S., et al. 2021, ApJ, 912, 46
Chen, T.-W., Yang, S., Srivastav, S., et al. 2025, ApJ, 983, 86
Christodoulou, E., de Wit, S., Bonanos, A. Z., et al. 2025, A&A, 704, A96
Chugai, N. N., Chevalier, R. A., & Utrobin, V. P. 2007, ApJ, 662, 1136
Chun, S.-H., Yoon, S.-C., Jung, M.-K., Kim, D. U., & Kim, J. 2018, ApJ, 853, 79
Clayton, M. 2018, PhD thesis, University of Oxford
Clayton, M., Podsiadlowski, P., Ivanova, N., & Justham, S. 2017, MNRAS, 470, 1788
Czesla, S., Schröter, S., Schneider, C. P., et al., 1906, PyA: Python astronomy-related packages, Astrophysics Source Code Library, ascl:1906.010
Davies, B., Crowther, P. A., & Beasor, E. R. 2018, MNRAS, 478, 3138
Davies, B., Kudritzki, R.-P., Plez, B., et al. 2013, ApJ, 767, 3
Decin, L., Richards, A. M. S., Marchant, P., & Sana, H. 2024, A&A, 681, A17
Dessart, L., & Hillier, D. J. 2019, A&A, 625, A9
Dessart, L., Hillier, D. J., Waldman, R., & Livne, E. 2013, MNRAS, 433, 1745
Dessart, L., & Jacobson-Galán, W. V. 2023, A&A, 677, A105
Dessart, L., Kotak, R., Jacobson-Galan, W., et al. 2025, A&A, 704, L6

Dessart, L., Livne, E., & Waldman, R. 2010, MNRAS, 408, 827
Dong, Y., Sand, D. J., Valenti, S., et al. 2023, ApJ, 957, 28
Draine, B. T., & Lee, H. M. 1984, ApJ, 285, 89
Ekström, S., Georgy, C., Eggenberger, P., et al. 2012, A&A, 537, A146
Ercolino, A., Jin, H., Langer, N., & Dessart, L. 2024, A&A, 685, A58
Ertini, K., Regna, T. A., Ferrari, L., et al. 2025, A&A, 699, A60
Falk, S. W., & Arnett, W. D. 1977, ApJS, 33, 515
Fang, Q., Moriya, T. J., Maeda, K., Dorozsmai, A., & Silva-Farfán, J. 2025, ApJ, 990, 60
Faran, T., Poznanski, D., Filippenko, A. V., et al. 2014a, MNRAS, 442, 844
Faran, T., Poznanski, D., Filippenko, A. V., et al. 2014b, MNRAS, 445, 554
Farrell, E. J., Groh, J. H., Meynet, G., & Eldridge, J. J. 2020, MNRAS, 494, L53
Ferrari, L., Folatelli, G., Ertini, K., et al. 2025, A&A, 703, A12
Foreman-Mackey, D., Hogg, D. W., Lang, D., & Goodman, J. 2013, PASP, 125, 306
Förster, F., Moriya, T. J., Maureira, J. C., et al. 2018, NatAs, 2, 808
Fouesneau, M. 2025, Pyphot, v1.6.0, Zenodo, doi:10.5281/zenodo.14712174
Fransson, C., Ergon, M., Challis, P. J., et al. 2014, ApJ, 797, 118
Fuller, J., & Tsuna, D. 2024, OJAp, 7, 47
Gal-Yam, A., Arcavi, I., Ofek, E. O., et al. 2014, Natur, 509, 471
Giorgini, J. D. & JPL Solar System Dynamics Group 1996, DPS, 28, 2504
Goldberg, J. A., & Bildsten, L. 2020, ApJL, 895, L45
Goldberg, J. A., Bildsten, L., & Paxton, B. 2019, ApJ, 879, 3
Goldberg, J. A., Bildsten, L., & Paxton, B. 2020, ApJ, 891, 15
Goldberg, J. A., Jiang, Y.-F., & Bildsten, L. 2022, ApJ, 929, 156
Goodman, J., & Weare, J. 2010, CAMCS, 5, 65
Guo, J. H., & Li, Y. 2002, ApJ, 565, 559
Gustafsson, B., Edvardsson, B., Eriksson, K., et al. 2008, A&A, 486, 951
Gutiérrez, C. P., Anderson, J. P., Hamuy, M., et al. 2017, ApJ, 850, 89
Harris, C. R., Millman, K. J., van der Walt, S. J., et al. 2020, Natur, 585, 357
Heger, A., Jeannin, L., Langer, N., & Baraffe, I. 1997, A&A, 327, 224
Hinds, K. R., Perley, D. A., Sollerman, J., et al. 2025, MNRAS, 541, 135
Hiramatsu, D., Tsuna, D., Berger, E., et al. 2023, ApJL, 955, L8
Hogg, D. W., Bovy, J., & Lang, D. 2010, arXiv:1008.4686
Hong, X., Sun, N.-C., Niu, Z., et al. 2024, ApJL, 977, L50
Hsu, B., Smith, N., Goldberg, J. A., et al. 2024, ApJ, 990, 148
Hueichapán, E., Cartier, R., Prieto, J. L., et al. 2025, arXiv:2508.02656
Hunter, J. D. 2007, CSE, 9, 90
Itagaki, K. 2023, TNSTR, 2023–1158, 1
Ivezic, Z., & Elitzur, M. 1997, MNRAS, 287, 799
Ivezic, Z., & Elitzur, M. 1999, MNRAS, 303, 864
Jacobson-Galán, W. V., Dessart, L., Davis, K. W., et al. 2025, ApJ, 992, 100
Jacobson-Galán, W. V., Dessart, L., Margutti, R., et al. 2023, ApJL, 954, L42
Jaynes, E. T. 1987, in Fundamental Theories of Physics, ed. C. R. Smith & G. J. Erickson, 21 (Springer)
Jencson, J. E., Pearson, J., Beasor, E. R., et al. 2023, ApJL, 952, L30
Josselin, E., Blommaert, J. A. D. L., Groenewegen, M. A. T., Omont, A., & Li, F. L. 2000, A&A, 357, 225
Joyce, M., Leung, S.-C., Molnár, L., et al. 2020, ApJ, 902, 63
Jurcevic, J. S., Pierce, M. J., & Jacoby, G. H. 2000, MNRAS, 313, 868
Kasen, D., & Woosley, S. E. 2009, ApJ, 703, 2205
Kilpatrick, C. D., Foley, R. J., Jacobson-Galán, W. V., et al. 2023, ApJL, 952, L23
Kippenhahn, R., Weigert, A., & Weiss, A. 2013, Stellar Structure and Evolution,
Kiss, L. L., Szabó, M., & Bedding, T. R. 2006, MNRAS, 372, 1721
Kozyreva, A., Caputo, A., Baklanov, P., Mironov, A., & Janka, H.-T. 2025, A&A, 694, A319
Kozyreva, A., Shingles, L., Mironov, A., Baklanov, P., & Blinnikov, S. 2020, MNRAS, 499, 4312
Langer, G. E. 1971, MNRAS, 155, 199
Laplace, E., Justham, S., Renzo, M., et al. 2021, A&A, 656, A58
Laplace, E., Schneider, F. R. N., & Podsiadlowski, P. 2025, A&A, 695, A71
Levesque, E. M., Massey, P., Olsen, K. A. G., et al. 2005, ApJ, 628, 973
Ma, J.-Z., Chiavassa, A., de Mink, S. E., et al. 2024, ApJL, 962, L36
Ma, J.-Z., Justham, S., Pakmor, R., et al. 2025, arXiv:2510.14875
Martinez, L., & Bersten, M. C. 2019, A&A, 629, A124
Montargès, M., Chiavassa, A., Kervella, P., et al. 2017, A&A, 605, A108
Montargès, M., Kervella, P., Perrin, G., et al. 2014, A&A, 572, A17
Moriya, T., Tominaga, N., Blinnikov, S. I., Baklanov, P. V., & Sorokina, E. I. 2011, MNRAS, 415, 199
Moriya, T. J., Subrayan, B. M., Milisavljevic, D., & Blinnikov, S. I. 2023, PASJ, 75, 634
Morozova, V., Piro, A. L., Renzo, M., et al. 2015, ApJ, 814, 63
Morozova, V., Piro, A. L., & Valenti, S. 2018, ApJ, 858, 15
Müller, B., Heger, A., Liptai, D., & Cameron, J. B. 2016, MNRAS, 460, 742
Neustadt, J. M. M., Kochanek, C. S., & Smith, M. R. 2024, MNRAS, 527, 5366
Niu, Z., Sun, N.-C., Maund, J. R., et al. 2023, ApJL, 955, L15
O'Gorman, E., Vlemmings, W., Richards, A. M. S., et al. 2015, A&A, 573, L1
Ossenkopf, V., Henning, T., & Mathis, J. S. 1992, A&A, 261, 567
Paxton, B., Bildsten, L., Dotter, A., et al. 2011, ApJS, 192, 3
Paxton, B., Cantiello, M., Arras, P., et al. 2013, ApJS, 208, 4
Paxton, B., Marchant, P., Schwab, J., et al. 2015, ApJS, 220, 15
Paxton, B., Schwab, J., Bauer, E. B., et al. 2018, ApJS, 234, 34
Paxton, B., Smolec, R., Schwab, J., et al. 2019, ApJS, 243, 10
Percy, J. R., & Khatu, V. C. 2014, JAVSO, 42, 1
Perley, D. A., Gal-Yam, A., Irani, I., & Zimmerman, E. 2023, TNSAN, 119, 1
Podsiadlowski, P., Joss, P. C., & Hsu, J. J. L. 1992, ApJ, 391, 246
Popov, D. V. 1993, ApJ, 414, 712
Qin, Y.-J., Zhang, K., Bloom, J., et al. 2024, MNRAS, 534, 271
Ransome, C. L., Villar, V. A., Tartaglia, A., et al. 2024, ApJ, 965, 93
Ren, Y., Jiang, B.-W., Yang, M., & Gao, J. 2019, ApJS, 241, 35
Sana, H., de Mink, S. E., de Koter, A., et al. 2012, Sci, 337, 444
Schneider, F. R. N., Laplace, E., & Podsiadlowski, P. 2025, A&A, 700, A253
Schneider, F. R. N., Podsiadlowski, P., & Laplace, E. 2024, A&A, 686, A45
Schneider, F. R. N., Podsiadlowski, P., & Müller, B. 2021, A&A, 645, A5
Sengupta, S., Sujit, D., & Sarangi, A. 2025, arXiv:2508.04497
Shrestha, M., DeSoto, S., Sand, D. J., et al. 2025, ApJL, 982, L32
Singh, A., Teja, R. S., Moriya, T. J., et al. 2024, ApJ, 975, 132
Smartt, S. J. 2015, PASA, 32, e016
Smartt, S. J., Eldridge, J. J., Crockett, R. M., & Maund, J. R. 2009, MNRAS, 395, 1409
Smith, N., Pearson, J., Sand, D. J., et al. 2023, ApJ, 956, 46
Soker, N. 2021, ApJ, 906, 1
Soker, N. 2023, RAA, 23, 081002
Soraisam, M. D., Szalai, T., Van Dyk, S. D., et al. 2023, ApJ, 957, 64
Stothers, R. 1969, ApJ, 156, 541
Stothers, R., & Leung, K. C. 1971, A&A, 10, 290
Suzuki, A., & Shigeyama, T. 2025, MNRAS, 543, 3929–3951
Temaj, D., Schneider, F. R. N., Laplace, E., Wei, D., & Podsiadlowski, P. 2024, A&A, 682, A123
Townsend, R. H. D., & Teitler, S. A. 2013, MNRAS, 435, 3406
van der Velden, E. 2020, JOSS, 5, 2004
Van Dyk, S. D., Srinivasan, S., Andrews, J. E., et al. 2024, ApJ, 968, 27
Vasylyev, S. S., Dessart, L., Yang, Y., et al. 2025, arXiv:2505.03975
Vinko, J., Bodola, Z. R., Godeny, A., et al. 2025, ApJ, 993, 39
Virtanen, P., Gommers, R., Oliphant, T. E., et al. 2020, NatMe, 17, 261
Woosley, S. E., Heger, A., & Weaver, T. A. 2002, RvMP, 74, 1015
Xiang, D., Mo, J., Wang, X., et al. 2024a, ApJL, 969, L15
Xiang, D., Mo, J., Wang, L., et al. 2024b, SCPMA, 67, 219514
Yang, M., Bonanos, A. Z., Jiang, B., et al. 2023, A&A, 676, A84
Yang, M., Bonanos, A. Z., Jiang, B.-W., et al. 2018, A&A, 616, A175
Yang, M., & Jiang, B. W. 2011, ApJ, 727, 53
Yang, M., & Jiang, B. W. 2012, ApJ, 754, 35
Yoon, S.-C., & Cantiello, M. 2010, ApJL, 717, L62
Zimmerman, E. A., Irani, I., Chen, P., et al. 2024, Natur, 627, 759